

ARTICLE TYPE

Multiscale modeling of linear elastic heterogeneous structures via localized model order reduction

Philipp Diercks^{*1} | Karen Veroy² | Annika Robens-Radermacher¹ | Jörg F. Unger¹

¹Department 7.7 Modeling and Simulation, Bundesanstalt für Materialforschung und -prüfung (BAM), Unter den Eichen 87, 12205 Berlin, Germany

²Centre for Analysis, Scientific Computing and Applications (CASA) Department of Mathematics and Computer Science, University of Eindhoven, P.O. Box 513, 5600 MB Eindhoven, The Netherlands

Correspondence

*Philipp Diercks, Unter den Eichen 87, 12205 Berlin, Germany, Email: philipp.diercks@bam.de

Present Address

Unter den Eichen 87, 12205 Berlin, Germany

Abstract

In this paper, a methodology for fine scale modeling of large scale linear elastic structures is proposed, which combines the variational multiscale method, domain decomposition and model order reduction. The influence of the fine scale on the coarse scale is modelled by the use of an additive split of the displacement field, addressing applications without a clear scale separation. Local reduced spaces are constructed by solving an oversampling problem with random boundary conditions. Herein, we inform the boundary conditions by a global reduced problem and compare our approach using physically meaningful correlated samples with existing approaches using uncorrelated samples. The local spaces are designed such that the local contribution of each subdomain can be coupled in a conforming way, which also preserves the sparsity pattern of standard finite element assembly procedures. Several numerical experiments show the accuracy and efficiency of the method, as well as its potential to reduce the size of the local spaces and the number of training samples compared to the uncorrelated sampling.

KEYWORDS:

Multiscale methods; variational multiscale method; localized model order reduction; proper orthogonal decomposition; domain decomposition methods

1 | INTRODUCTION

1.1 | Multiscale modeling and model order reduction

Many problems in science and engineering involve multiple scales. With large heterogeneities present in spatial scales, it is often insufficient to assume a homogeneous material in the analysis of a mechanical structure. For example, the dispersed phases (particles or fibers) in a composite material may lead to fluctuations in the displacement field which cannot be captured by the

phenomenological macroscale model. Therefore, in analyzing large scale structures, it is necessary to take into account the materials' fine scale heterogeneity to more accurately model the structure's behaviour.

It is often sufficient to predict macroscopic properties of the multiscale system based on a representative volume element (RVE) that preserves the geometrical complexity of the heterogeneous microstructure and accurately predicts effective material parameters. Approaches based on computational homogenization, such as the FE^2 method (see e. g. ^{1,2,3,4}) mitigate the issue of computational cost compared to full fine scale simulations, but the nested solution procedure is still a demanding task. Therefore, many approaches^{5,6,7,8} combining the FE^2 approach with model reduction of the fine scale problem exist. These approaches rest on the assumption of *separation of scales* and the existence of an RVE; however, this is not the case in many applications, e. g. for composite structures where simply the dimension of the fine scale features is not much smaller than the macroscopic dimension, therefore breaking the MMM-principle defined in⁹, or in the presence of macroscopic cracks emerging from the localization of microdefects^{10,11}.

Thus, methods which address both scales simultaneously are needed. Standard multiscale methods have emerged from the variational approaches to numerical homogenization, such as the variational multiscale method (VMM)^{12,13} or the multiscale finite element method (MsFEM)¹⁴, which aim for a correction or stabilization of the conventional (coarse grid) discretization by including (unresolved) fine scale information into the global problem. Important developments of the VMM include the works by M. Larson and A. Målqvist^{15,16,17} and the local orthogonal decomposition (LOD)¹⁸. For a more detailed discussion on the history of numerical homogenization in the absence of a clear separation of scales we refer to Altmann et al.¹⁹.

In addition, the significant increase in computational cost entailed with the resolution of the fine scale features in the numerical model makes the direct solution of the problem infeasible. In this work, this is addressed by the use of model order reduction techniques (see the textbooks^{20,21} for an introduction to the topic). The high dimensional numerical problem (also termed high-fidelity approximation or full order model (FOM)) is replaced by a reduced order model (ROM) of small dimension, which is achieved by the projection of the original system of equations upon a low-dimensional subspace of the high-dimensional space in which the solution lives. A key point is the construction of the reduced basis, which spans the low dimensional subspace, from a set of suitably selected high-fidelity solutions. In (now standard) reduced basis (RB) methods, the so-called snapshots are selected via the weak greedy algorithm^{22,23}. Another popular method for subspace construction is the proper orthogonal decomposition (POD)^{24,25}. However, efficient reduction of nonlinear problems in mechanics still poses a challenge due to the repeated evaluation of the nonlinear operator over the full domain. Among others, well-known techniques to address this issue are the empirical interpolation method (EIM)²⁶ and its discrete variant²⁷, the hyper-reduction^{28,29}, the energy-conserving sampling and weighting method^{30,31} or the empirical cubature method³². Moreover, more recent approaches^{33,34} make use of machine learning methods to construct ROMs for nonlinear problems.

In the case of full fine scale simulations, limitations of established model order reduction techniques become apparent; examples of such limitations include prohibitively large reduced spaces due to high dimensional parameter spaces or computationally expensive offline phases due to large computational domains. To alleviate these shortcomings, methods combining multiscale methods, domain decomposition and model order reduction were developed. Approaches of this kind are known as *localized model order reduction methods*, and an extensive review is given by Buhr et al.³⁵. The main idea is the construction of local reduced spaces on subdomains, i. e. parts of the global domain, which are then coupled (either in a conforming or non-conforming way) to obtain a global approximation.

1.2 | Contributions and relation to previous work

In this work, we aim to provide a computationally efficient framework for multiscale modeling of linear heterogeneous structures that is able to incorporate localization phenomena as described in section 1.1. While this contribution is limited to the linear case, we suggest an approach that addresses both scales simultaneously and flexibly, with a view towards future extensions to nonlinear material behaviour.

The proposed methodology features an additive split of the displacement field into coarse and fine scale parts, based on the VMM. The coarse scale basis functions are computed directly by extending standard finite element shape functions on the boundary of local subdomains into the interior of the respective subdomains. Local approximation spaces for the fine scale part are constructed by exploiting possible fine scale solutions for a coarse grid element using the concept of oversampling first introduced in the context of the MsFEM¹⁴. To this end, a so-called transfer eigenvalue problem^{36,37} (or oversampling problem) yielding local reduced spaces which are optimal in the sense of Kolmogorov is solved and the associated transfer operator is approximated by random sampling³⁸. The novelty consists in the use of a *multivariate normal* distribution with non-zero mean given by the solution of a reduced global problem, and a covariance matrix with squared exponential kernel to sample the random boundary conditions. To this end, algorithm 1 of³⁸ is modified to inform the boundary conditions of the oversampling problem by the solution of a reduced global problem, incorporating the macroscopic displacement state of the structure of interest into the training data. Note that a similar approach to build local reduced spaces using interface basis functions (Lagrangian or Fourier bases) as boundary conditions was proposed in Iapichino et al.³⁹. The difference is that Iapichino et al. prescribed these interface basis functions on the boundary of the subdomain of interest directly. In our approach, the macroscopic displacement state of the global structure of interest is prescribed on the boundary of the oversampling domain, making it more suitable for the construction of reduced spaces tailored to the solution of the partial differential equation (PDE) in that area of the domain. Moreover, we further restrict the fine scale solutions obtained from the oversampling problem to the edges of the target subdomain and construct a reduced fine scale edge basis, separately for each edge in the partition of the global domain. Then, the fine scale edge basis functions are again extended into the interior of the respective subdomains. We note that such a procedure to construct

a conforming, localized reduced order approximation is outlined in a more general form in the review by Buhr et al.³⁵. Finally, the fine scale subdomain basis functions are problem-dependent local functions which are continuous on subdomain boundaries and thus yield a conforming approximation. This decomposition of the fine scale part in its respective edge parts is favorable since the resulting discrete equation system of the (global) ROM preserves the sparsity pattern and computational complexity of standard finite element methods.

In view of future extensions of the method to the nonlinear case, we expect that the impact of incorporating the local deformation state of the structure of interest in the construction of the local reduced basis will be more significant. Also, the amplitude of the boundary conditions prescribed in the oversampling problem is relevant in nonlinear problems which may be challenging in the case of random boundary conditions. Due to the resemblance of the constructed empirical fine scale basis functions with hierarchical FE shape functions (see e.g.⁴⁰), it is then possible to incorporate strategies from the field of adaptive refinement (p -refinement).

As an alternative to the decomposition outlined above, the generalized finite element method (GFEM)^{41,42,43} can be used to construct a global approximation from local reduced spaces. To this end, local reduced basis functions are multiplied with standard finite element shape functions to create a partition of unity.

The remainder of this article is organised as follows. First, in section 2, the problem setting and full order model are described. The proposed method is explained in section 3, comprising the construction of local approximation spaces in section 3.1 and the assembly of the reduced order model in section 3.2. Numerical examples illustrating the performance of the suggested approach are discussed in section 4. Concluding remarks and an outlook are given in section 5.

2 | PROBLEM SETTING AND MODELING

While the method could be applied to other linear PDEs, only the balance of linear momentum in the static case on a large computational domain $\Omega_{\text{gl}} \subset \mathbb{R}^d$ (the suffix ‘gl’ stands for global) is considered, with boundary $\partial\Omega_{\text{gl}} = \Sigma_{\text{N}} \cup \Sigma_{\text{D}}$, where Σ_{N} and Σ_{D} denote Neumann and Dirichlet boundaries, respectively, and $d = 2, 3$ is the spatial dimension. Without loss of generality, volumetric forces are neglected, and the displacement solution \mathbf{u}_{gl} is sought such that

$$\begin{aligned} -\nabla \cdot \boldsymbol{\sigma}(\nabla \mathbf{u}_{\text{gl}}) &= 0 \quad \text{in } \Omega_{\text{gl}}, \\ \boldsymbol{\sigma}(\nabla \mathbf{u}_{\text{gl}}) \cdot \mathbf{n} &= \hat{\mathbf{t}} \quad \text{on } \Sigma_{\text{N}}, \\ \mathbf{u}_{\text{gl}} &= \mathbf{g}_{\text{D}} \quad \text{on } \Sigma_{\text{D}}. \end{aligned} \tag{1}$$

Here the Cauchy stress tensor $\boldsymbol{\sigma}$ for one of the M material components of the heterogeneous linear elastic material is given by

$$\boldsymbol{\sigma}_m = \lambda_m^1 (\varepsilon(\mathbf{u}_{\text{gl}}) \cdot \mathbb{1}) \mathbb{1} + 2\lambda_m^2 \varepsilon(\mathbf{u}_{\text{gl}}), \quad \text{with } m = 1, \dots, M, \tag{2}$$

where λ_m^1 and λ_m^2 are Lamé's constants. The linear strain operator is denoted by $\varepsilon(\mathbf{v}) = \frac{1}{2} (\nabla \mathbf{v} + \nabla \mathbf{v}^T)$. Moreover, \mathbf{n} is the body's surface outward normal vector, $\hat{\mathbf{t}}$ is the traction given on the Neumann boundary Σ_N and $\hat{\mathbf{u}}$ is the displacement prescribed on the Dirichlet boundary Σ_D . We define $\mathbf{u}_{\text{gl}} = \mathbf{u}_0 + \mathbf{u}_D$, with a suitable *dirichlet lift* $\mathbf{u}_D \in \mathbb{V}_D = \{\mathbf{v} \in [H^1(\Omega_{\text{gl}})]^d : \mathbf{v} = \mathbf{g}_D \text{ on } \Sigma_D\}$ in case of inhomogeneous Dirichlet boundary conditions. The weak form for eq. (1) reads: find $\mathbf{u}_0 \in \mathbb{V} = \{\mathbf{v} \in [H^1(\Omega_{\text{gl}})]^d : \mathbf{v} = \mathbf{0} \text{ on } \Sigma_D\}$ such that

$$a(\mathbf{u}_{\text{gl}}, \mathbf{v}) = f(\mathbf{v}), \quad \forall \mathbf{v} \in \mathbb{V}, \quad (3)$$

where

$$a(\mathbf{w}, \mathbf{v}) = \sum_{m=1}^M \int_{\Omega_{\text{gl}}^m} \lambda_m^1 \text{tr}(\varepsilon(\mathbf{w})) \text{tr}(\varepsilon(\mathbf{v})) + 2\lambda_m^2 \varepsilon(\mathbf{w}) \cdot \cdot \varepsilon(\mathbf{v}) \, dV \quad (4)$$

and

$$f(\mathbf{v}) = \int_{\Sigma_N} \hat{\mathbf{t}} \cdot \mathbf{v} \, dA - a(\mathbf{u}_D, \mathbf{v}). \quad (5)$$

Here, Ω_{gl}^m is used to indicate the parts of the global domain associated with the different phases of the heterogeneous material. Note that, $\text{tr}(\bullet)$ denotes the trace of a tensor and ' $\cdot \cdot$ ' stands for the scalar product of two 2nd-order tensors (2-fold contraction as defined in section 2.1.15 of⁴⁴). The energy inner product and energy norm are defined as

$$(\mathbf{w}, \mathbf{v})_{\mathbb{V}} = a(\mathbf{w}, \mathbf{v}), \quad \forall \mathbf{w}, \mathbf{v} \in \mathbb{V}, \quad (6)$$

$$\|\mathbf{v}\|_{\mathbb{V}}^2 = a(\mathbf{v}, \mathbf{v}), \quad \forall \mathbf{v} \in \mathbb{V}. \quad (7)$$

2.1 | Full order model

The *direct numerical solution* or *full order model* is defined as the finite element approximation of eq. (3), searching for the solution in a high fidelity discrete space $\mathbb{V}_{\delta} \subset \mathbb{V}$: find $\mathbf{u}_{\delta} \in \mathbb{V}_{\delta} \subset \mathbb{V}$, such that

$$a(\mathbf{u}_{\delta}, \mathbf{v}) = f(\mathbf{v}), \quad \forall \mathbf{v} \in \mathbb{V}_{\delta}. \quad (8)$$

The dimension of the discrete space is denoted by $N_{\delta} = \dim(\mathbb{V}_{\delta})$, and we denote by $\{\phi_i\}_{i=1}^{N_{\delta}}$ a standard finite element basis of \mathbb{V} such that, the stiffness matrix and right hand side can be written as

$$(\mathbf{A}_{\delta})_{ij} = a(\phi_j, \phi_i), \quad (\mathbf{f}_{\delta})_i = f(\phi_i). \quad (9)$$

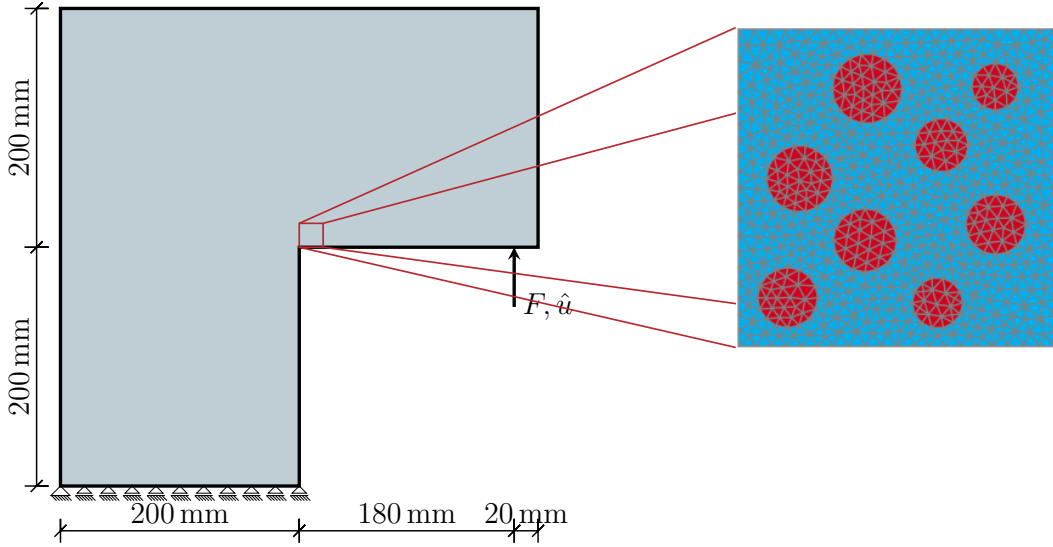


Figure 1 L-shaped panel test specimen and exemplary fine scale structure.

3 | MULTISCALE METHOD

Every material is intrinsically multiscale. In the framework of continuum mechanics, often the assumption of a homogeneous material to solve macroscale problems is sufficient. However, it is only a homogenized approximation of the underlying finer scales and thus not suitable in loading conditions where the real physical phenomena on the fine scale greatly influence the macroscopic behaviour. Consider for example the propagation of a crack in the test specimen shown in fig. 1, which is only tractable by resolving the fine scale in the numerical model. The macroscopic approximation then needs to be improved by fine scale functions taking into account fluctuations in the displacement field due to the heterogeneous fine scale structure. Note that the discretization of the fine scale structure might vary over the whole mesoscale structure.

Following this line of thought, we introduce an additive split of the displacement solution as in the VMM^{12,13} $\mathbf{u}_0 = \mathbf{u}_c + \mathbf{u}_f$ and (in analogy to section 2) the Hilbert space

$$\mathbb{V} = \mathbb{V}_c \oplus \mathbb{V}_f, \quad (10)$$

is introduced, such that

$$a(\mathbf{u}_c, \mathbf{v}_c) + a(\mathbf{u}_f, \mathbf{v}_c) = f(\mathbf{v}_c) \quad \forall \mathbf{v}_c \in \mathbb{V}_c, \quad (11)$$

$$a(\mathbf{u}_c, \mathbf{v}_f) + a(\mathbf{u}_f, \mathbf{v}_f) = f(\mathbf{v}_f) \quad \forall \mathbf{v}_f \in \mathbb{V}_f. \quad (12)$$

Here $(\bullet)_c$ denotes the coarse scale part and $(\bullet)_f$ the fine scale part. The corresponding discrete spaces are associated with coarse scale and fine scale partitions of the domain Ω_{gl} as depicted in fig. 2. It is assumed that the global domain can be decomposed into N_c non-overlapping subdomains denoted by Ω_i , $i = 1, 2, \dots, N_c$. Within each subdomain Ω_i , the computational domain for

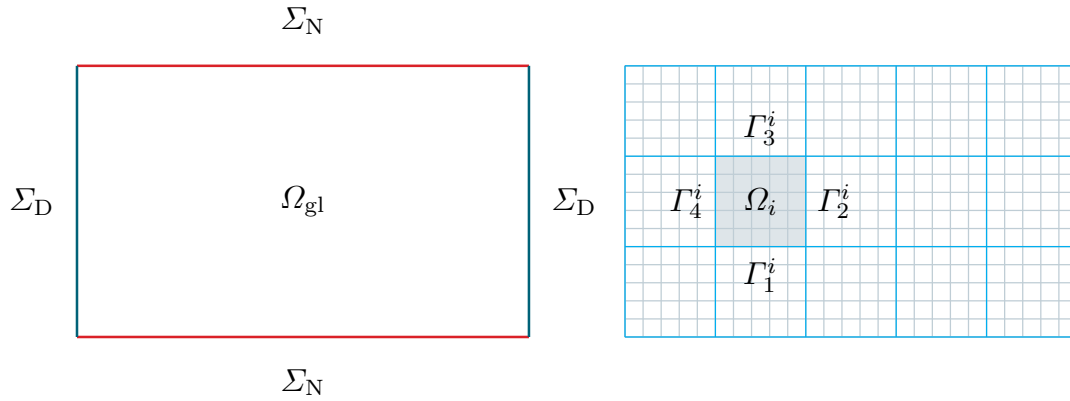


Figure 2 Exemplary computational domain Ω_{gl} on the left and coarse scale (blue lines) and fine scale (gray lines) grid partition on the right. A subdomain Ω_i and its edges Γ_e^i are also shown.

each of the material phases is denoted by Ω_i^m with $m = 1, \dots, M$ in analogy to the definitions in section 2. Furthermore, the subdomain boundaries are denoted by Γ_e^i , with $e = 1, 2, 3, 4$ referring to the respective bottom, right, top and left edge of the subdomain. Analogously, the global space \mathbb{V} is decomposed into subdomain spaces \mathbb{V}_i with dimension $n_\delta^i = \dim(\mathbb{V}_i)$,

$$\mathbb{V} = \bigoplus_{i=1}^{N_c} \mathbb{V}_i. \quad (13)$$

Section 3.1 deals with the construction of reduced basis functions which yield a good approximation of \mathbf{u}_{gl} , such that the PDE eq. (1) is locally fulfilled on Ω_i . The definition of the global approximation is described in section 3.2.

3.1 | Construction of local approximation spaces

In this section, the construction of the reduced basis functions for the coarse scale, $\{\boldsymbol{\varphi}_i\}_{i=1}^{n_c}$, and for the fine scale, $\{\boldsymbol{\psi}_i\}_{i=1}^{n_f}$, is addressed. The proposed *offline phase* consists of three stages:

1. direct calculation of coarse scale basis $\{\boldsymbol{\varphi}_i\}_{i=1}^{n_c}$,
2. calculation of fine scale edge basis functions $\{\boldsymbol{\chi}_i^e\}_{i=1}^{n_{\text{mpe}}}$, where n_{mpe} denotes the number of modes per (subdomain) edge; via two approaches:
 - (a) by solving an oversampling problem (leading to an *empirical* basis),
 - (b) by constructing *hierarchical* finite element shape functions h_{p+1} (see e. g. chapter 8 in⁴⁰) of degree $p + 1$, where p is the polynomial degree of the Legendre polynomial $P_p(\xi)$,

$$h_{p+1} = \int P_p(\xi) d\xi, \quad \text{with } P_p(\xi) = \frac{1}{(p-1)!} \frac{1}{2^{p-1}} \frac{d^p}{d\xi^p} [(\xi^2 - 1)^p], \quad (14)$$

3. calculation of fine-scale subdomain basis functions $\{\boldsymbol{\psi}_i\}_{i=1}^{n_f}$ from $\{\boldsymbol{\chi}_i^e\}_{i=1}^{n_{\text{mpe}}}$.

Note that, in the remainder of this article, we refer to the set of coarse scale basis functions and fine-scale subdomain basis functions constructed from hierarchical finite element shape functions as the *hierarchical basis*. The set of coarse scale basis functions and fine scale subdomain basis functions constructed from empirical fine scale edge basis functions is referred to as *empirical basis*. In the latter case, we study two different sampling strategies to generate training sets, drawing samples either from a *correlated* or *uncorrelated* sampling distribution, both of which are defined in section 3.1.4.

3.1.1 | Direct calculation of coarse scale basis functions

The coarse scale basis is required to form a partition of unity on the subdomain boundary $\partial\Omega_i$, to enable the assembly procedure described in section 3.2. Therefore, we choose piecewise bilinear functions to approximate the coarse scale part, such that the fine scale part vanishes at the vertices of the coarse scale grid, similar to the hierarchical shape functions. By extending standard finite element shape functions on the boundary of the subdomain into the interior of the respective subdomain, the effect of the differential operator in the interior is also incorporated in the coarse scale basis functions. The coarse scale basis functions are defined as the solution of

$$a_i(\boldsymbol{\varphi}_j, \mathbf{v}) = 0, \quad \boldsymbol{\varphi}_j = \boldsymbol{\Phi}_j \text{ on } \partial\Omega_i, \quad \forall \mathbf{v} \in \mathbb{V}_i, \quad (15)$$

where

$$a_i(\mathbf{w}, \mathbf{v}) = \sum_{m=1}^M \int_{\Omega_i^m} \lambda_m^1 \text{tr}(\boldsymbol{\varepsilon}(\mathbf{w})) \text{tr}(\boldsymbol{\varepsilon}(\mathbf{v})) + 2\lambda_m^2 \boldsymbol{\varepsilon}(\mathbf{w}) \cdot \boldsymbol{\varepsilon}(\mathbf{v}) \, dV \quad (16)$$

and $\boldsymbol{\Phi}_j$ being the standard Lagrange basis functions, which are constructed from Lagrange ploynomials (see⁴⁰)

$$l_k^q(\xi) = \frac{(\xi - \xi_0)(\xi - \xi_1) \cdots (\xi - \xi_{k-1})(\xi - \xi_{k+1}) \cdots (\xi - \xi_q)}{(\xi_k - \xi_0)(\xi_k - \xi_1) \cdots (\xi_k - \xi_{k-1})(\xi_k - \xi_{k+1}) \cdots (\xi_k - \xi_q)}, \quad (17)$$

giving unity at ξ_k and passing through q points. In two dimensions, the node j of the coarse grid element may be labeled by its column and row number, I, J ,

$$\boldsymbol{\Phi}_j = l_I^q(\xi) l_J^r(\eta). \quad (18)$$

The integer q and r stand for the number of subdivisions in each direction and ξ and η for the reference coordinates. For quadrilateral coarse grid cells in the two dimensional case and linear interpolation in the coarse scale, this yields a local coarse scale basis of size $n_c = 8$, which is used in the remainder of the article.

3.1.2 | Calculation of fine scale edge basis functions

As mentioned in the beginning of section 3.1, two different approaches are considered. The fine scale edge basis functions may be defined as *hierarchical* shape functions a priori. In this case, no precomputation is required and one could directly compute the extension of the edge basis into the interior of the subdomain, as described in section 3.1.3. The construction of the

empirical fine scale edge basis poses the main challenge in the proposed framework. In order to exploit fine scale solutions of the PDE eq. (1) on any subdomain Ω_i , we make use of the concept of oversampling¹⁴. First, the oversampling domain $\hat{\Omega}$ is defined, such that $\Omega_i \subsetneq \hat{\Omega} \subset \Omega_{\text{gl}}$. Furthermore, the distance between the boundary $\partial\Omega_i$ and $\Gamma_\mu := \partial\hat{\Omega} \setminus \partial\Omega_{\text{gl}}$ is greater than zero, i. e. $\text{dist}(\Gamma_\mu, \partial\Omega_i) \geq \rho > 0$ for some ρ . Depending on the configuration for a particular Ω_i , $\Gamma_N := \partial\hat{\Omega} \cap \Sigma_N$ or $\Gamma_D := \partial\hat{\Omega} \cap \Sigma_D$ may be not empty and Neumann or Dirichlet boundary conditions of the global problem need to be considered in the oversampling as well. In order to sufficiently incorporate Dirichlet and Neumann boundary conditions in the reduced basis functions, several oversampling problems have to be defined. We also refer to the different oversampling problems as “configurations” due to the possible change in topology and boundary conditions for each problem. The challenge in solving eq. (1) on $\hat{\Omega}$ lies in the definition of the boundary data on Γ_μ which is used to exploit possible solutions of the PDE on Ω_i . Taking, for example, parametric boundary conditions on Γ_μ , for a specific numerical discretization, the maximum size of the parameter space \mathbb{P} is the number of degrees of freedom on Γ_μ . Consider for example $\hat{\Omega}$ as a 3×3 block of mesoscale subdomains, as shown in fig. 3. With the subdomain type I, discretized with 11 vertices per edge, as shown in fig. 4a, this leads to 120 vertices on Γ_μ . For linear triangular elements, this would lead to a parameter space $\mathbb{P} = \mathbb{R}^{240}$, where a dense uniform sampling as usually done in standard greedy approaches (see²³) is infeasible. For this reason, Buhr and Smetana³⁸ suggest to solve eq. (1) on $\hat{\Omega}$ with random boundary conditions on Γ_μ (i. e. , the associated transfer operator \mathbf{T} is approximated by random sampling). Note, that the transfer operator \mathbf{T} maps functions on the boundary Γ_μ to the solution of the PDE on the target subdomain Ω_i . As an example, fig. 3 shows the oversampling domain $\hat{\Omega}$ for a subdomain of interest Ω_i that is entirely inside the structure.

In this work, we adopt “Algorithm 1: Adaptive Randomized Range Approximation”³⁸ and modify it to include the solution of a global reduced problem in the training data. In section 4, we then compare the randomized approach using an *uncorrelated* sampling strategy with the proposed *correlated* sampling strategy. More details on the different sampling strategies are discussed in section 3.1.4. For ease of notation, we assume that there exists a suitable training set $\mathcal{S}_{\text{train}}$ containing samples generated using either of the aforementioned sampling strategies.

The *oversampling problem*

$$\begin{aligned}
 -\nabla \cdot \boldsymbol{\sigma}(\nabla \mathbf{u}) &= 0 && \text{in } \hat{\Omega}, \\
 \boldsymbol{\sigma}(\nabla \mathbf{u}) \cdot \mathbf{n} &= \mathbf{0} && \text{on } \Gamma_N, \\
 \mathbf{u} &= \mathbf{0} && \text{on } \Gamma_D, \\
 \mathbf{u} &= \mathbf{g} && \text{on } \Gamma_\mu, \forall \mathbf{g} \in \mathcal{S}_{\text{train}},
 \end{aligned} \tag{19}$$

is then solved for \mathbf{u} for each element $\mathbf{g} \in \mathcal{S}_{\text{train}}$ in the training set prescribed on the boundary Γ_μ . In case of inhomogeneous Dirichlet data \mathbf{g}_D on Σ_D , the fine scale part $\mathbf{g}_f = \mathbf{g}_D - \mathbf{g}_c$ is set as the basis for the respective edges. The coarse scale part $\mathbf{g}_c = \sum_{i=1}^{n_c} \mathbf{g}_j \boldsymbol{\varphi}_i$ is given as a linear combination of the function value of \mathbf{g} at the j -th vertex of the coarse grid cell and the coarse scale basis functions defined in section 3.1.1. In case of non-zero Neumann data $\hat{\mathbf{t}} \neq \mathbf{0}$, the fine scale edge basis is extended by

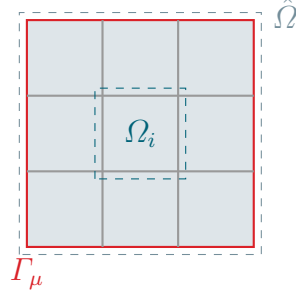


Figure 3 Oversampling domain $\hat{\Omega}$, target subdomain Ω_i , and the boundary Γ_μ for a target subdomain in the interior of the structure are shown.

additional edge functions obtained by solving the problem

$$\begin{aligned} -\nabla \cdot \sigma(\nabla u) &= 0 & \text{in } \hat{\Omega}, \\ \sigma(\nabla u) \cdot \mathbf{n} &= \hat{\mathbf{t}} & \text{on } \Gamma_N, \\ \mathbf{u} &= \mathbf{0} & \text{on } \Gamma_\mu. \end{aligned} \quad (20)$$

The computational procedure to construct the fine scale edge basis functions which consists of repeatedly solving eq. (19) for different training samples is summarized in algorithm 1.

Following Buhr and Smetana³⁸, we let \mathcal{P} be the probability, $P_{\text{span}(\mathbf{B})}$ the orthogonal projection onto $\text{span}(\mathbf{B})$, N_T the rank of the transfer operator \mathbf{T} and $\lambda_{\min}^{M_s}$ the smallest eigenvalue of the matrix of the inner product in the source space of the transfer operator. First, a set of edge basis functions \mathbf{B}_e and n_t testvectors \mathbf{M}_e for each edge e of the target subdomain Ω_i are initialized. The test data consists in solutions of eq. (19) with uncorrelated random samples \mathbf{g} (drawn from a multivariate normal distribution with zero mean and covariance matrix $\Sigma = \mathbb{1}$) prescribed as boundary data on Γ_μ . The restriction of the solution to the target subdomain Ω_i is equivalent to the image of the transfer operator \mathbf{T} and hence the restriction of the solution to one of the edges of the target subdomain is denoted as $\mathbf{T}\mathbf{g}|_{\Gamma_e^i}$. For each of the testvectors in \mathbf{M}_e the coarse scale part is subtracted. Next, the error estimator factor c_{est} is determined based on the chosen inner products. The body of the while loop consists in drawing a new sample using the chosen sampling strategy (either *uncorrelated* or *correlated*), computing the solution to eq. (19) and restricting it to the edges of the target subdomain. Subsequently, the coarse scale part is subtracted and each edge basis function set \mathbf{B}_e is extended by adding the fine scale part of the solution and orthonormalizing the edge basis using the modified Gram-Schmidt algorithm. In the last step, the set of testvectors for each edge is orthogonalized with respect to the edge basis set. This way, with increasing number of iterations the norm of each of the testvectors in the test sets \mathbf{M}_e is decreased until the criterion to terminate the while loop is met. If the criterion for one of the edges is met before the others, the algorithm is continued without adding basis functions for that particular edge. The fine scale edge basis is denoted as $\{\chi_j^e\}_{j=1}^{n_{\text{mpe}}^e}$, with $e = 1, 2, 3, 4$ referring to one of the edges of the subdomain Γ_e^i and n_{mpe}^e denoting the number of modes per edge for a particular edge e .

Algorithm 1 Modified Adaptive Randomized Range Approximation

```

1: function ADAPTIVERANDRANGEAPPROX( $T, \text{tol}, n_t, \varepsilon_{\text{algofail}}$ )
    Input: Operator  $T$ , target tolerance  $\text{tol}$ , number of testvectors  $n_t$ , maximum failure probability  $\varepsilon_{\text{algofail}}$ , training set  $S_{\text{train}}$ 
    Output: Fine scale edge basis  $B_e$  for each of the edges  $\Gamma_e^i$  of the target subdomain  $\Omega_i$  where each edge basis fulfills
     $R^n = \text{span}(B_e)$  with property  $\mathcal{P}(\|T - P_{R^n}T\| \leq \text{tol}) > (1 - \varepsilon_{\text{algofail}})$ 
2:    $B_e \leftarrow \emptyset$  ▷ initialize basis for each edge
3:    $M_e \leftarrow \{Tg^1|_{\Gamma_e^i}, \dots, Tg^{n_t}|_{\Gamma_e^i}\}$  ▷ initialize test vectors for each edge
4:    $M_e \leftarrow M_e - M_e^c$  ▷ subtract coarse scale part
5:    $\varepsilon_{\text{testfail}} \leftarrow \varepsilon_{\text{algofail}}/N_T$ 
6:    $c_{\text{est}} \leftarrow \left[ \sqrt{2\lambda_{\min}^{M_s}} \text{erf}^{-1} \left( \sqrt{\varepsilon_{\text{testfail}}} \right) \right]^{-1}$  ▷ determine error estimator factor
7:   while  $(\max_{t \in M_e} \|t\|_R) \cdot c_{\text{est}} > \text{tol}$  do ▷ compare maxnorm to target tol for each test set
8:      $g \leftarrow \text{draw sample from training set } S_{\text{train}}$ 
9:      $u \leftarrow Tg|_{\Gamma_e^i}$  ▷ restriction of the solution to each edge
10:     $u_f \leftarrow u - u_c$ 
11:     $B_e \leftarrow B_e \cup \{u_f\}$ 
12:     $B_e \leftarrow \text{orthonormalize}(B_e)$ 
13:     $M_e \leftarrow \{t - P_{\text{span}(B_e)}t \mid t \in M_e\}$  ▷ orthogonalize test vectors to span( $B_e$ )
14:  end while
15:  return  $B_e$ 
16: end function

```

3.1.3 | Calculation of fine scale subdomain basis functions

The final step in constructing the reduced basis for the fine scale part of the displacement solution consists in the extension of the edge basis functions into the respective subdomain Ω_i . It is important to note that, by setting the same function on a single edge for adjacent subdomains, continuity of the global approximation is ensured. Furthermore, to enable the standard assembly procedure as in the finite element method, in the local extension problem, it is necessary to enforce zero boundary conditions on edges $\partial\Omega_i \setminus \Gamma_e^i$ where the basis function is not prescribed. For each edge Γ_e^i , with $e = 1, 2, 3, 4$, and each mode in the set of edge basis functions $\{\chi_j^e\}_{j=1}^{n_{\text{mpe}}^e}$, find the subdomain basis function ψ_j^e such that

$$a_i(\psi_j^e, v) = 0, \quad \forall v \in \mathbb{V}_i, \quad (21)$$

$$\text{with } \psi_j^e = \chi_j^e \text{ on } \Gamma_e^i \text{ and } \psi_j^e = \mathbf{0} \text{ on } \partial\Omega_i \setminus \Gamma_e^i,$$

where the bilinear form $a_i(\cdot, \cdot)$ is given by eq. (16). All $n_f = \sum_{e=1}^4 n_{\text{mpe}}^e$ solutions of eq. (21) are then gathered in one set of fine scale basis functions

$$\{\psi_j\}_{j=1}^{n_f} = \{\psi_k^1\}_{k=1}^{n_{\text{mpe}}^1} \cup \{\psi_k^2\}_{k=1}^{n_{\text{mpe}}^2} \cup \{\psi_k^3\}_{k=1}^{n_{\text{mpe}}^3} \cup \{\psi_k^4\}_{k=1}^{n_{\text{mpe}}^4}. \quad (22)$$

3.1.4 | Sampling distributions

In this section, the two different choices (sampling strategies considered) for the definition of the training set S_{train} mentioned in section 3.1.2 are discussed.

In the first variant, *uncorrelated* samples are used to define the random boundary conditions in the oversampling problem. Following Buhr and Smetana³⁸, we use the term “random normal vector” to “denote a vector whose entries are independent and identically distributed random variables with normal distribution”. Each entry g_i of the vector $\mathbf{g} \in \mathcal{S}_{\text{train}}$ is sampled from a normal distribution with zero mean and variance of one, which is denoted as

$$g_i \sim \mathcal{N}(0, 1). \quad (23)$$

Note that throughout the manuscript, we use the term *uncorrelated* to refer to the random samples which are drawn from a normal distribution with zero mean and variance of one.

In the second variant, *correlated* samples are drawn from a *multivariate normal* distribution with the solution of the global reduced problem \mathbf{u}_c as mean. The solution \mathbf{u}_c is obtained by solving the reduced order model (see section 3.2) using only the coarse scale basis.

$$\mathbf{g} \sim \mathcal{N}(\mathbf{u}_c, \boldsymbol{\Sigma}). \quad (24)$$

Here, $\boldsymbol{\Sigma}$ denotes the covariance matrix of the distribution. The covariance matrix

$$\boldsymbol{\Sigma} = \mathbf{M} \mathbf{P} \mathbf{M} \quad (25)$$

is computed based on the matrix \mathbf{P} with elements $p_{ij} = \exp(-d_{ij}/L_{\text{corr}})$ which defines the correlation of two entries g_i and g_j of \mathbf{g} based on the euclidean distance d_{ij} between the points associated with the entries in \mathbf{g} and the matrix $\mathbf{M} = \text{diag}(\mathbf{u}_c)$. L_{corr} is the correlation length and controls the strength of correlation between two points. Note that throughout the manuscript, we use the term *correlated* to refer to the random samples, which are drawn from a multivariate normal distribution with \mathbf{u}_c as mean and covariance matrix $\boldsymbol{\Sigma}$ as described above.

In the limit $L_{\text{corr}} \rightarrow 0$, the correlation matrix \mathbf{P} becomes the identity $\mathbb{1}$, and hence the same result as training the basis with the fully uncorrelated samples is to be expected. Therefore, for the examples presented in section 4, the correlation length is first set to the maximum Euclidean distance between two points of the oversampling domain. This effectively includes the correlated, smoother macroscopic states in the training. The number of eigenvalues of $\boldsymbol{\Sigma}$ whose values are greater than 5% of the largest eigenvalue, is taken as the number of samples to be drawn using this correlation length. The tolerance on the eigenvalues, which results in limiting the number of samples per correlation length, is used to prevent drawing fully dependent samples. Subsequently, the correlation length is halved and the number of samples to be drawn using the updated correlation length is determined based on the relative tolerance on the number of eigenvalues of $\boldsymbol{\Sigma}$ minus the number of already drawn samples. This way, the strength of the correlation decreases with increasing number of samples drawn in the range finder algorithm (algorithm 1). By decreasing the correlation length, we aim at drawing as many less correlated samples as necessary to achieve a sufficiently good approximation of the range of the transfer operator, as would have been the case when using fully uncorrelated samples from the start.

3.2 | Reduced order model

The proposed approach features a local basis $\{\xi_k\}_{k=1}^n = \{\varphi_i\}_{i=1}^{n_c} \cup \{\psi_j\}_{j=1}^{n_f}$, with n being the maximum number of basis functions, which constitutes a partition of unity for all vertices of the coarse grid and is continuous on subdomain boundaries Γ_e^i . Here φ_i and ψ_j are the n_c coarse scale and n_f fine scale functions, respectively. The local reduced basis can be expressed in the standard finite element basis ϕ_j associated with the fine grid

$$\xi_k = \sum_{j=1}^{n_\delta} B_{jk} \phi_j, \quad (26)$$

where the k -th column of the matrix $\mathbf{B} \in \mathbb{R}^{n_\delta \times n}$ holds the coefficients of the k -th basis function. The local contribution of a subdomain is then given by

$$\mathbf{A}_n = \mathbf{B}^T \mathbf{A}_\delta^{\text{loc}} \mathbf{B}, \quad \mathbf{f}_n = \mathbf{B}^T \mathbf{f}_\delta^{\text{loc}}, \quad (27)$$

where $\mathbf{A}_\delta^{\text{loc}} \in \mathbb{R}^{n_\delta \times n_\delta}$ and $\mathbf{f}_\delta^{\text{loc}} \in \mathbb{R}^{n_\delta}$ denote the stiffness matrix and external force vector, respectively, of a subdomain. Note that unless body forces are present, $\mathbf{f}_\delta^{\text{loc}}$ is zero in case $\Gamma_e^i \cap \Sigma_N = \emptyset$ or $\hat{\mathbf{t}} = \mathbf{0}$ which is the case for most subdomains. Due to the above-mentioned properties of the reduced basis functions, the local contributions $\mathbf{A}_n \in \mathbb{R}^{n \times n}$ and $\mathbf{f}_n \in \mathbb{R}^n$ can be sorted into global vectors following the usual assembly procedure of standard finite elements, where each node, edge and face (3D) is associated with a fixed number of degrees of freedom (DoFs). The global system of the *reduced order model* of size $N \ll N_\delta$ is then written as

$$\mathbf{A}_N \mathbf{u}_N = \mathbf{f}_N, \quad (28)$$

where $\mathbf{A}_N \in \mathbb{R}^{N \times N}$, $\mathbf{f}_N \in \mathbb{R}^N$ and N is the number of unknown DoFs in the reduced order model.

4 | NUMERICAL EXPERIMENTS

In this section, the performance of the empirical bases, using either the uncorrelated samples or the correlated samples (see section 3.1.4), is studied and compared to the hierarchical basis as a naïve choice for the approximation of the fine scale part. We also note that a comparison of Legendre basis functions and an empirical basis was carried out by Eftang and Patera in the context of port reduction for static condensation procedures⁴⁵. In section 4.1, a block example is implemented to illustrate the basic features of the proposed methodology. Next, a beam under the state of pure bending is analyzed for varying ratios of the elastic moduli as a measure for the heterogeneity, and the empirical basis' performance is shown to be superior to that of the hierarchical basis for ratios greater than one. The applicability of the method to more complex problems (containing a stress singularity in this case) is demonstrated by the example of an L-shaped panel in section 4.3. Finally, details on the basis construction and the computational time of the FOM as well as offline and online phase of the ROM are given in section 4.4.

Table 1 Material parameters (taken from table 4 in⁴⁶).

	Mortar matrix	Aggregates
Young's modulus	$E_m = 30\,000 \text{ MPa}$	$E_a = 60\,000 \text{ MPa}$
Poisson ratio	$\nu_m = 0.2$	$\nu_a = 0.2$

The material parameters are given in table 1. Triangular elements with quadratic shape functions are implemented for the fine grid discretization of the mesoscale subdomain types used in the examples, as shown in fig. 4. Figure 5 shows the results of the mesh convergence analysis carried out for the mesoscale subdomains studied in the examples. For different levels of refinement, eq. (3) is solved on the mesoscale subdomain with boundary data given by eq. (32), and the error relative to a reference solution computed on the finest mesh is measured in the energy norm. The mesh is regarded as converged if the relative error in the energy norm is below one percent which leads to the discretizations as shown in fig. 4.

In all examples, the global error relative to the *full order model* (eq. (3)) is computed as follows. The absolute error on subdomain Ω_i defined as $\mathbf{e}_i = (\mathbf{u}_{\text{fom}})_i - (\mathbf{u}_{\text{rom}})_i$ is measured in the H^1 -norm as

$$\|\mathbf{e}_i\|_{V_i}^2 = \int_{\Omega_i} \mathbf{e}_i \cdot \mathbf{e}_i + \nabla \mathbf{e}_i \cdot \nabla \mathbf{e}_i \, dV. \quad (29)$$

The global absolute error is thus given by the square root of the sum of the squared local norm

$$\|\mathbf{e}\|_V = \sqrt{\sum_{i=1}^{N_c} \|\mathbf{e}_i\|_{V_i}^2}. \quad (30)$$

Analogously, the global relative error is given by

$$\frac{\|\mathbf{e}\|_V}{\|\mathbf{u}_{\text{fom}}\|_V} = \frac{\sqrt{\sum_{i=1}^{N_c} \|\mathbf{e}_i\|_{V_i}^2}}{\sqrt{\sum_{i=1}^{N_c} \|(\mathbf{u}_{\text{fom}})_i\|_{V_i}^2}}. \quad (31)$$

Furthermore, in each of the examples statistics over 20 realizations for each of the sampling approaches are given.

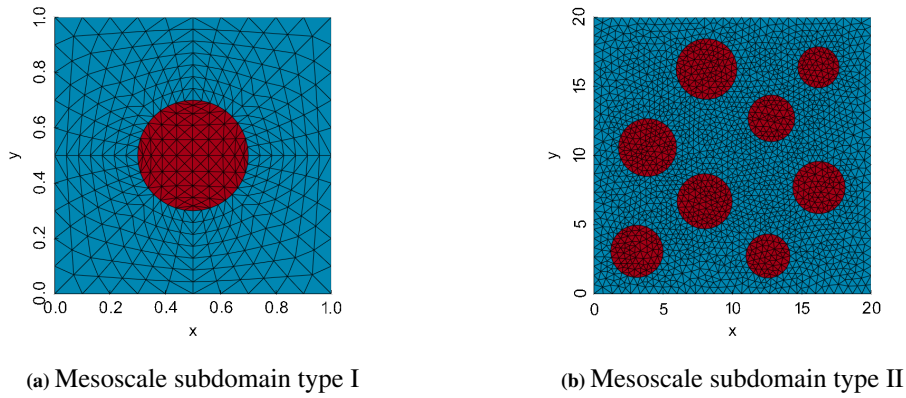


Figure 4 Mesoscale structures used in the examples.

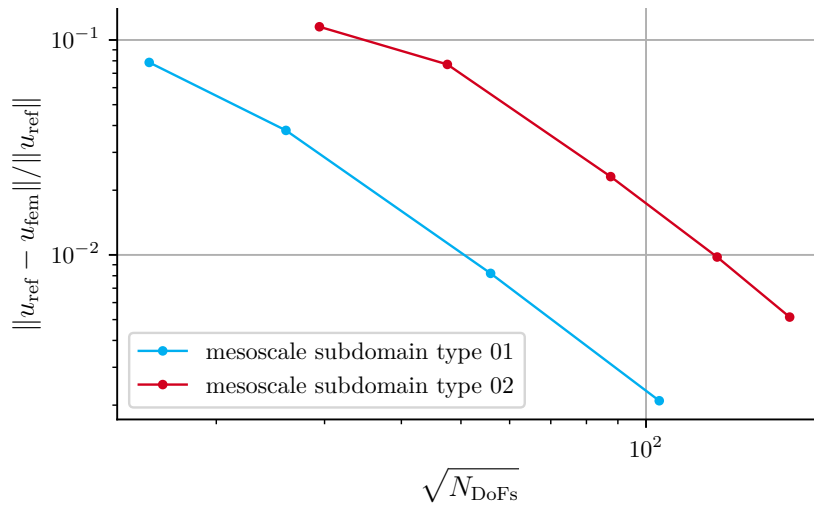


Figure 5 Relative error in the energy norm against square root of number of degrees of freedom in the mesh convergence analysis.

4.1 | Block example

In this example, eq. (1) is solved on a global domain $\Omega_{\text{gl}} = (0, 5)^2$ with Dirichlet data on the boundary $\Sigma_D := \partial\Omega_{\text{gl}}$ given in index notation by

$$u_i^D = a_{ij}x_j + b_{ij}x_j^2, \quad a_{ij}, b_{ij} \in \mathbb{R}. \quad (32)$$

The coefficients a_{ij} and b_{ij} are random variables sampled from a uniform distribution over $[0, 1)$ and scaled such that $\|\mathbf{u}^D(x_1 = 5, x_2 = 5)\| = 1$. The mesoscale subdomain of type I (fig. 4a) is used for each of the 25 subdomains, consequently, the coarse grid is chosen as a structured grid with five cells in each spatial direction, as shown in fig. 6.

While the performance of the empirical basis using the correlated samples is compared to the empirical basis using the uncorrelated samples, the target tolerance as input to the range finder algorithm algorithm 1 is varied. The decay of the relative

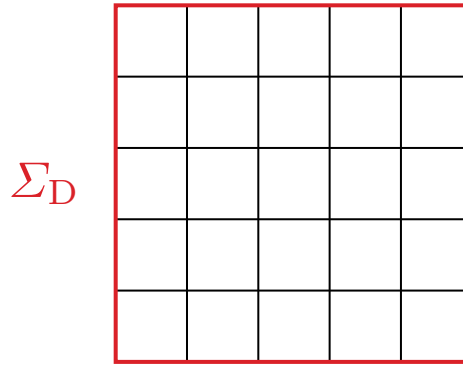


Figure 6 Illustration of the coarse grid discretization of the block example.

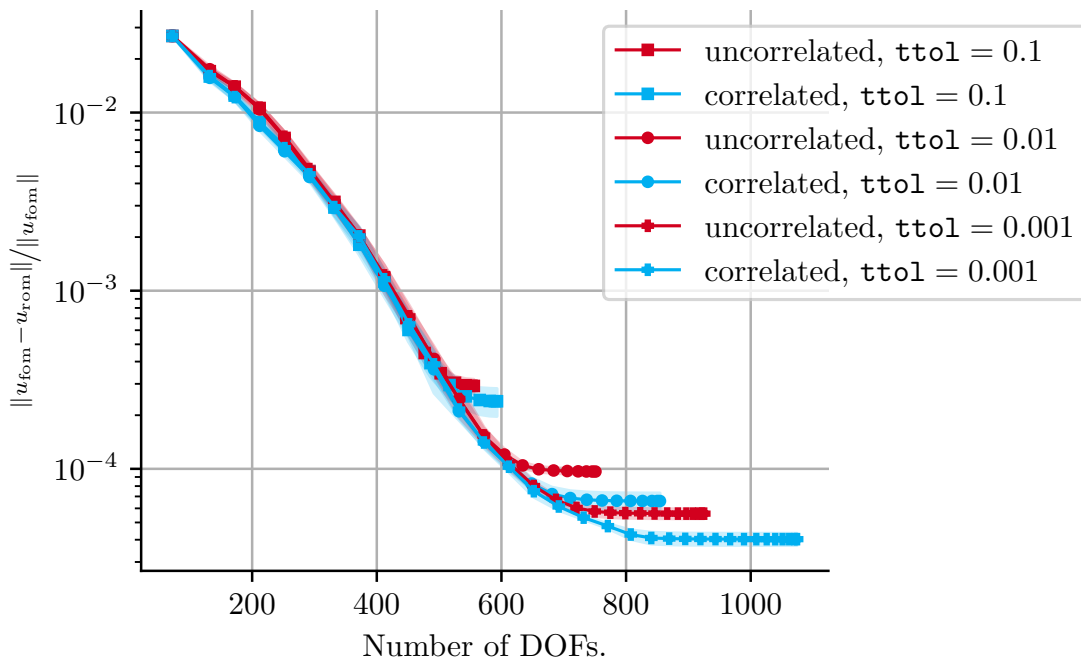


Figure 7 Block example: global relative error in the H^1 -norm for different sampling distributions and target tolerances (ttol). The values are averaged over the number of 20 realizations. The shaded areas indicate the standard deviation of the global relative error.

global error against the number of degrees of freedom in the ROM as shown in fig. 7, is computed as follows. For a given target tolerance, the fine scale basis functions are computed by solving N_c (number of subdomains) oversampling problems. Then the ROM is repeatedly evaluated and compared to the FOM while the number of fine scale basis functions per edge is increased (if possible) until the maximum number of basis functions is reached. The global relative ROM error is calculated as described by eqs. (29) to (31) in section 4.

In this example, the difference between the two sampling approaches is small, as the curves lie almost on top of each other. In both cases the error stagnates with increasing number of DoFs which is due to the fact that the maximum number of basis

functions varies per edge. The accuracy of the global approximation is thus limited by the worst approximation of the solution on one of the edges (presumably the edge with the lowest number of basis functions generated by algorithm 1). Moreover, as stated in³⁸, depending on the size of the oversampling domain and the choice of the inner products, the a posteriori error bound can be rather pessimistic and more basis functions than needed to achieve the target tolerance are generated.

For one of the realizations, the number of fine scale basis functions per edge obtained prescribing a target tolerance of $\text{ttol} = 0.001$ is shown for both sampling distributions in fig. 8. Only a single mode is necessary on the edges of the boundary of the domain, to account for the inhomogeneous Dirichlet boundary conditions. For both distributions, the number of fine scale basis functions in the interior is higher than for edges close to the boundary of the domain.

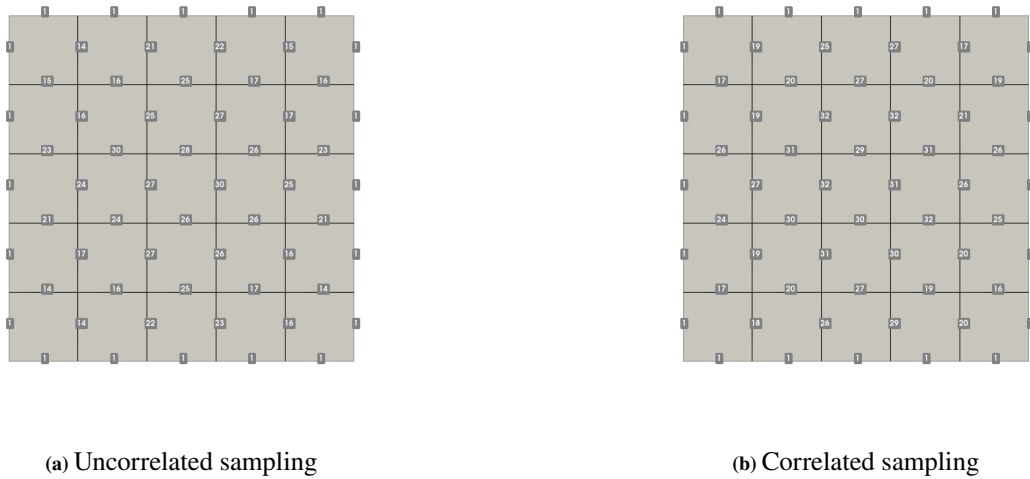
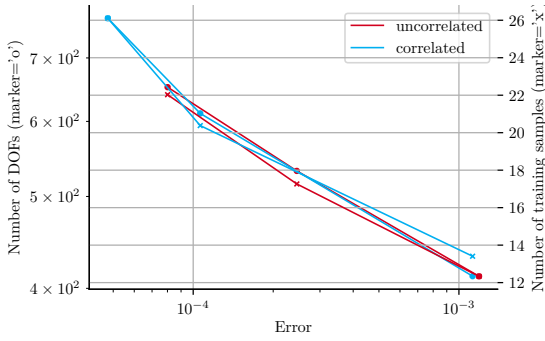


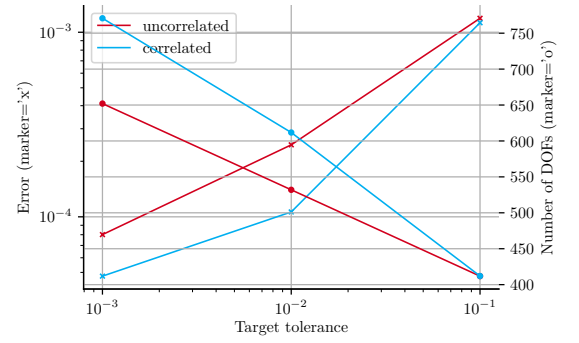
Figure 8 Block example: number of basis functions per edge generated by algorithm 1 for different sampling distributions and a target tolerance $\text{ttol} = 0.001$. The values are given for a specific realization.

Furthermore, using the correlated samples the number of modes per edge that are generated is generally larger. In this case, the criterion to exit the range finder algorithm (algorithm 1) is met after a larger number of training samples, which results in a more accurate approximation, but also larger number of DoFs in the global ROM (compare e. g. the relative error and number of DoFs for a target tolerance of $\text{ttol} = 0.01$ in fig. 9). However, fig. 9a shows, that to achieve a global relative error of e. g. $1 \cdot 10^{-4}$ on average about the same number of training samples are needed for both sampling approaches.

Finally, fig. 10 shows the absolute displacement error for particular realizations. For the same number of fine scale basis functions (and in this case also number of DoFs in the global ROM), the displacement field in the interior is better approximated when using the correlated samples, although the overall quality of the approximation is the same.

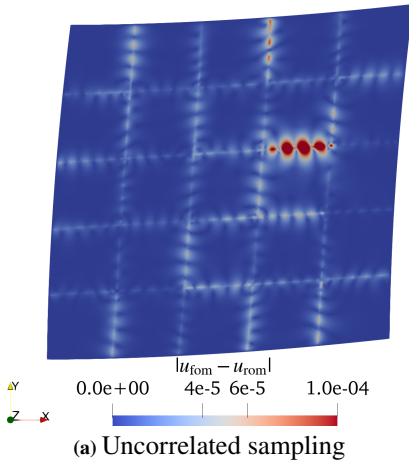


(a) Number of DOFs and training samples against mean global relative error. The number of training samples is averaged over the number of oversampling problems.

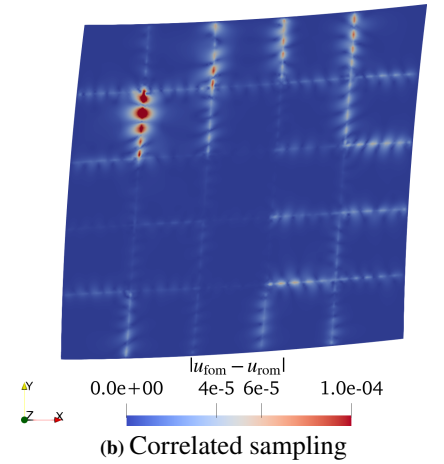


(b) Mean global relative error and number of DOFs against target tolerance ttol .

Figure 9 Results for the block example using the maximum number of modes per edge.



(a) Uncorrelated sampling



(b) Correlated sampling

Figure 10 Absolute displacement error for a particular realization with different sampling distributions in the deformed placement using 10 fine scale basis functions per edge. In both cases, a scale factor of 1 is used for the deformation and the domain is scaled by the ROM displacement solution.

4.2 | Beam example

A beam under the state of pure bending is considered on the domain $\Omega_{\text{gl}} = (0, L) \times (0, c)$ with length L , height c , and thickness $t = 1$ mm as illustrated in fig. 11a. The bending moment $M = 20rc^2$ MPa results from a horizontal distributed force $f_x = t \left(\frac{240y}{c} - 120 \right) t$ MPa, such that the analytical solution (according to⁴⁷) in the case of a homogeneous isotropic and linear

elastic material is

$$\sigma_{xx} = \left(\frac{240y}{c} - 120 \right) \text{ MPa}, \quad \sigma_{yy} = \tau_{xy} = 0 \text{ MPa}, \quad (33)$$

$$u = \left(\frac{240}{c} xy - 120x \right) \frac{\text{MPa}}{E}, \quad (34)$$

$$v = -\frac{\nu}{E} \left(\frac{120}{c} y^2 - 120y \right) \text{ MPa} - \frac{1}{E} \frac{120}{c} x^2 \text{ MPa}. \quad (35)$$

In this example, the empirical basis (using the correlated as well as the uncorrelated sampling approach) is compared to the hierarchical basis for varying ratios E_a/E_m of Young's moduli of the aggregates and matrix.

The dimensions of the beam $L = 1000$ mm and $c = 100$ mm are chosen such that the coarse grid consists of 50×5 mesoscale subdomains of type II, see fig. 4b. Therefore, oversampling problems which take into account the Dirichlet and Neumann boundary conditions are considered in the offline phase which is illustrated in fig. 11b. For each patch (oversampling domain) that contains one of the coarse grid cells marked blue, the associated oversampling problem needs to take into account the homogeneous Dirichlet boundary conditions. Analogously, for coarse grid cells marked red inhomogeneous Neumann boundary conditions need to be considered.

The oversampling domain $\hat{\Omega}_1, \hat{\Omega}_2, \hat{\Omega}_3, \hat{\Omega}_4$ and $\hat{\Omega}_5$, with their respective target subdomain $\Omega_1, \Omega_2, \Omega_3, \Omega_4$ and Ω_5 are shown in fig. 12 to illustrate the change in topology.



Figure 11 Schematic representation (a) of the beam problem and coarse grid discretization showing configurations to be considered in the offline phase.

For varying ratios E_a/E_m of Young's moduli for the aggregates and matrix, the global relative error is shown in fig. 13. It is referred to section 4.1 for details on the calculation of the global relative error.

In the homogeneous case, i.e. $E_a/E_m = 1$, the hierarchical basis results in a nested finite element method and the analytical solution can be exactly represented using only two basis functions per edge. However, for ratios $E_a/E_m > 1$, the hierarchical basis does not yield a good approximation of the fine scale part of the displacement, whereas the relative error decays much faster in case of the empirical basis. Moreover, in this particular example, the relative error decays at a higher rate using the correlated sampling approach compared to the uncorrelated sampling approach. For the approximation of the macroscopic state of pure bending only few basis functions are needed. Also, as mentioned in section 4.1, the algorithm tends to generate more

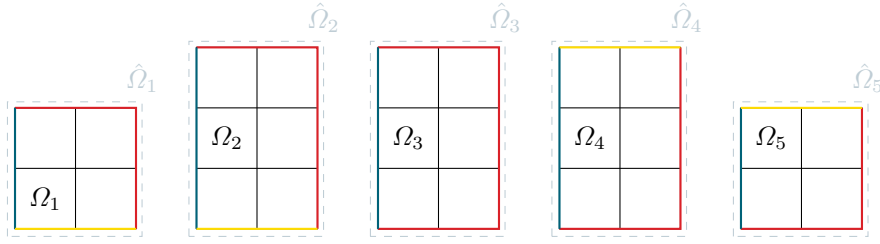


Figure 12 The configurations of the oversampling domain $\hat{\Omega}$ for the subdomains $\Omega_1, \Omega_2, \Omega_3$ on the left Dirichlet boundary in case of the beam example. The colors indicate the boundaries Σ_D (blue), Σ_N (yellow) and Γ_μ (red) whose topology is changing.

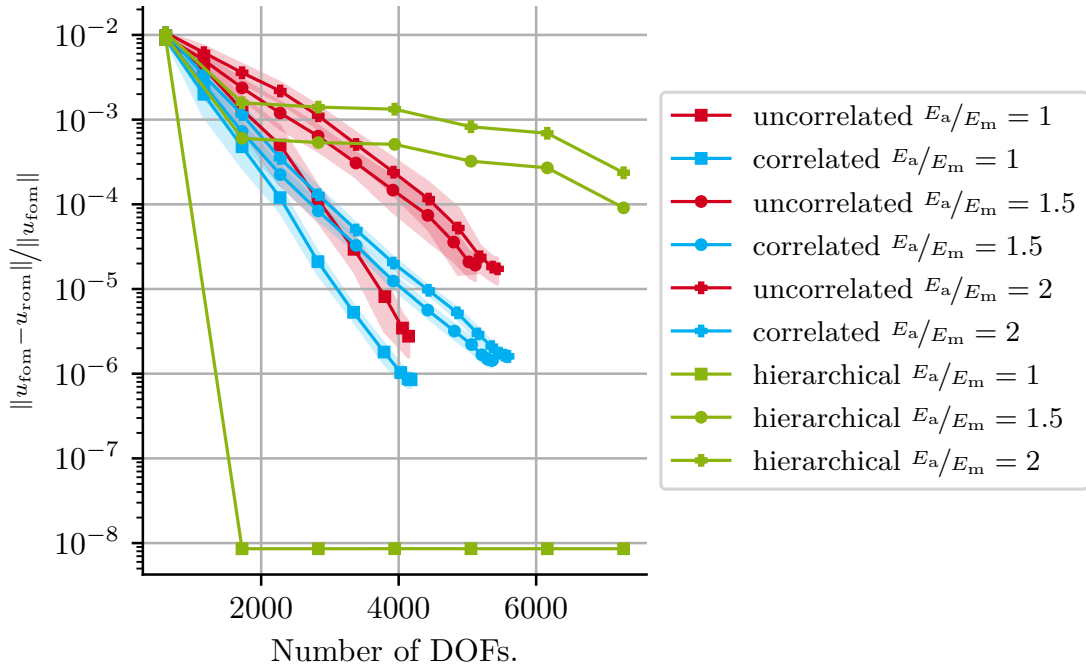


Figure 13 Beam example: global relative error in the H^1 -norm against number of degrees of freedom. The empirical basis (correlated and uncorrelated sampling approach both with target tolerance $\text{ttol} = 0.1$) and hierarchical basis are compared for varying ratios of Young's moduli. Regarding the randomized approaches, the average values over the number of 20 realizations and the standard deviation (shaded) of the global relative error are displayed.

basis functions than would have been necessary to achieve the target tolerance on the projection error and this effect seems to be even stronger in case of the correlated samples, as the relative error is almost a factor 10 (for $E_a/E_m = 2$) smaller than the error obtained using the uncorrelated samples.

Furthermore, the purpose of this example is to illustrate the effect of the heterogeneity on the displacement field, by comparing the hierarchical edge basis functions to the empirical fine scale edge basis functions. Therefore, the hierarchical edge basis functions are plotted in fig. 14 and the x - and y -components of the empirical edge basis functions (correlated sampling approach) for a particular subdomain in the interior of the global domain and its bottom edge are plotted in the figs. 15 and 16. The referenced figures show that for the homogeneous material the empirical fine scale edge functions share features similar to the ones of the

hierarchical shape functions. In the heterogeneous case the overall shape of at least the first mode is still similar, although a clear effect of the heterogeneity can be seen, which is also stronger for the higher modes.

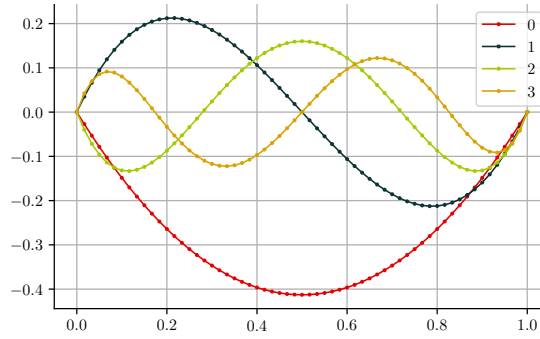


Figure 14 Illustration of the hierarchical fine scale edge basis functions.

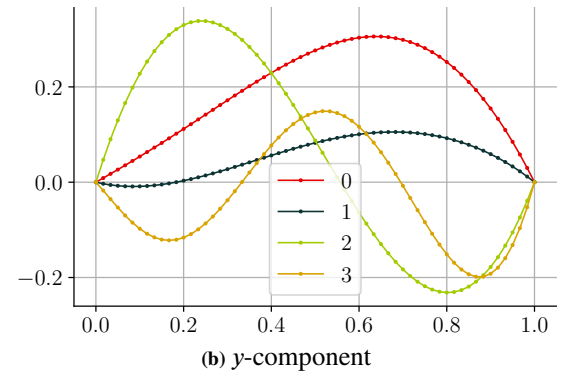
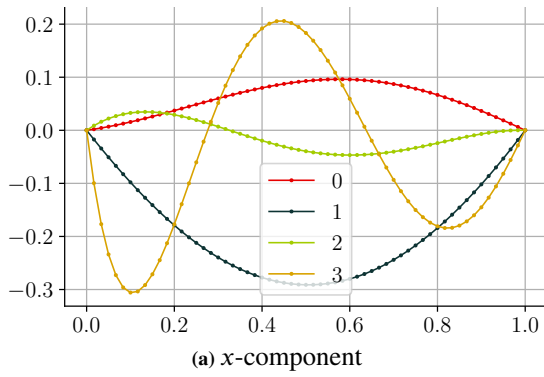


Figure 15 Fine scale edge basis for the empirical basis generated with correlated samples, $\text{ttol} = 0.1$ and $E_a/E_m = 1$.

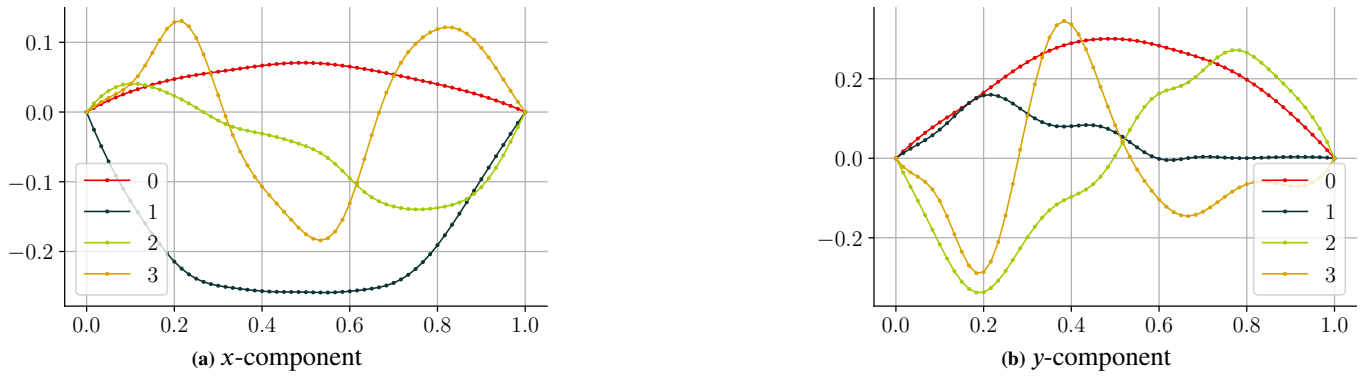


Figure 16 Fine scale edge basis for the empirical basis generated with correlated samples, $\text{ttol} = 0.1$ and $E_a/E_m = 2$.

4.3 | L-panel example

The third example is an L-shaped panel, see fig. 17a. It features a more complex geometry and a concentrated load modeled as a Neumann boundary condition. For simplicity, the load is modeled as a linearly varying hat function with maximum value $t_y = 200 \text{ N/mm}^2$ distributed over two coarse grid cells, such that the maximum vertical displacement is $u_y \approx 5.4 \text{ mm}$. Mesoscale subdomain type II (see fig. 4b) is used, leading to the coarse grid and configurations as shown in fig. 17b. The different configurations are encoded by color in the same manner as in the beam example (section 4.2). In case of the L-Panel, the correlated sampling approach is compared to the uncorrelated sampling approach for the empirical basis. The decay of the global relative error is shown in fig. 18 and the basis generated with correlated samples performs better for a smaller number of degrees of freedom (smaller number of fine scale edge modes). For a target tolerance of $\text{ttol} = 0.1$ using the correlated sampling approach more basis functions are generated, but the error of the global approximation compared to the FOM is smaller. In contrast, for smaller target tolerances, after reaching a certain accuracy of the approximation, more and more basis functions are generated for specific subdomains (edges) due to the pessimistic error estimator of algorithm 1 without improving the global error. This effect is more pronounced for the correlated sampling approach compared to the uncorrelated sampling approach.

However, fig. 19 shows the trend that the same approximation error can be achieved with less training samples in the offline phase and a smaller number of degrees of freedom in the ROM in the online phase when using the correlated sampling approach. Compare, e. g. the number of DoFs and training samples to achieve a global relative error of $1 \cdot 10^{-4}$ (fig. 19a) and the global relative error for both distributions for a number of DoFs of (i) 4000 and (ii) 7000 (fig. 19b). Moreover, fig. 20 shows the absolute displacement error for both sampling approaches using a maximum of 12 fine scale basis functions per edge. While the overall level of accuracy is the same, using the correlated sampling approach does improve the approximation near the recessed corner, which is known to be the critical area of the structure. On the contrary, the solution near the Neumann boundary is better approximated using the basis constructed from uncorrelated samples.

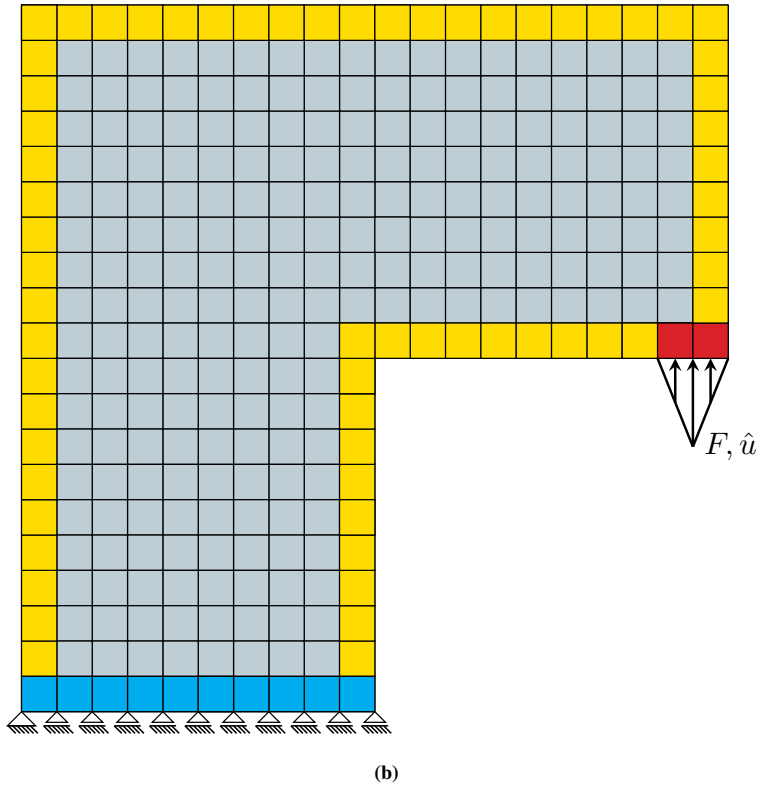
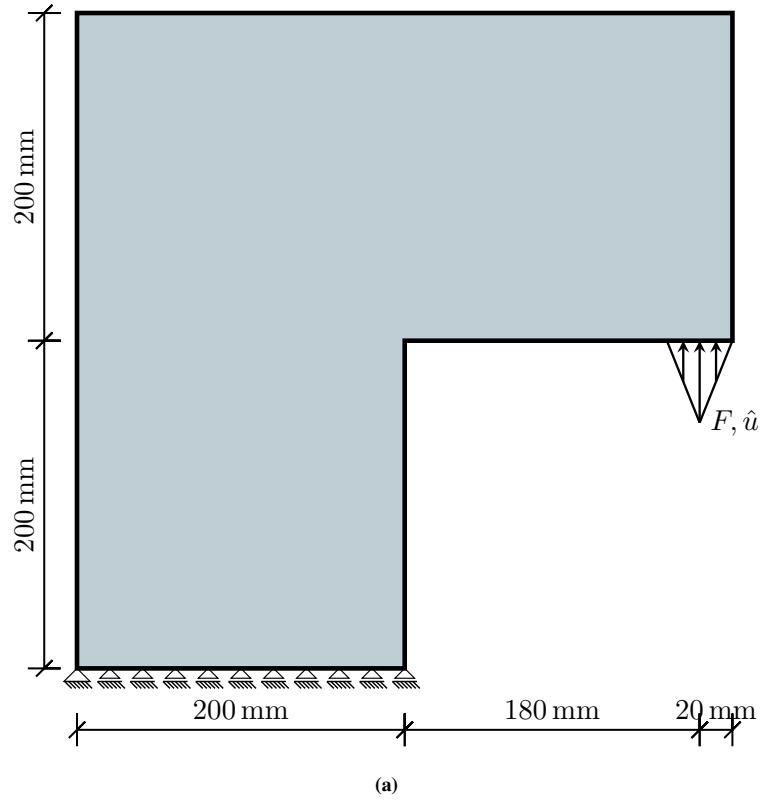


Figure 17 Schematic representation (a) and different configurations present in the chosen coarse grid (b) of the L-Panel example.

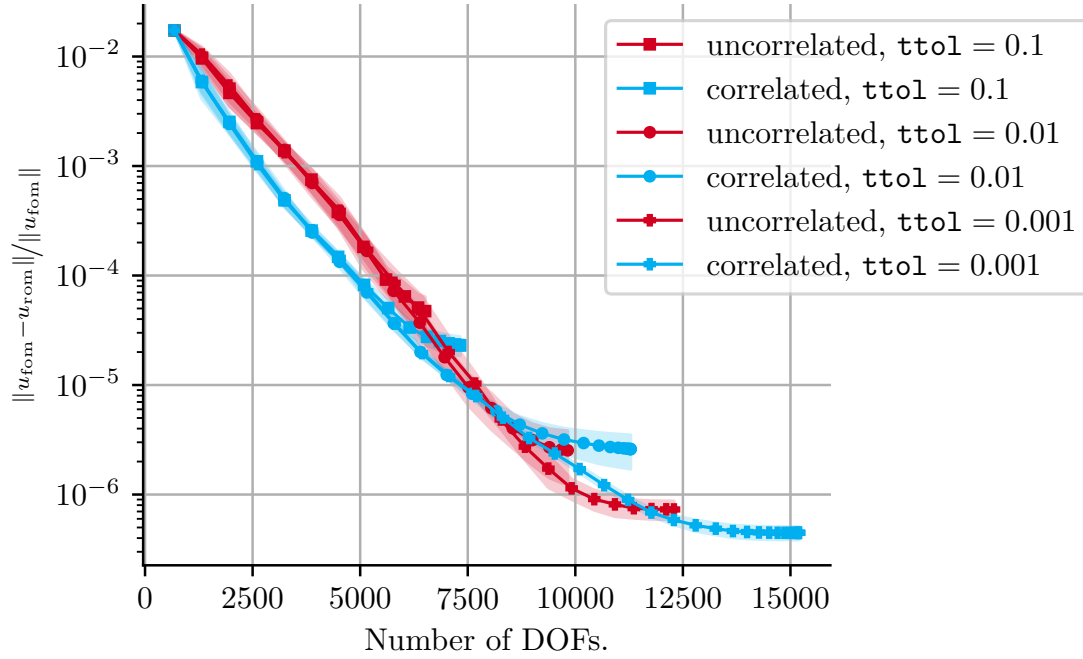
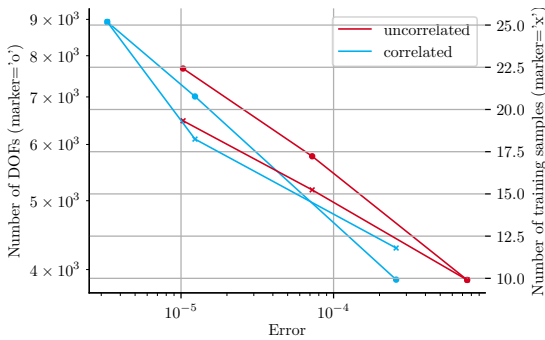
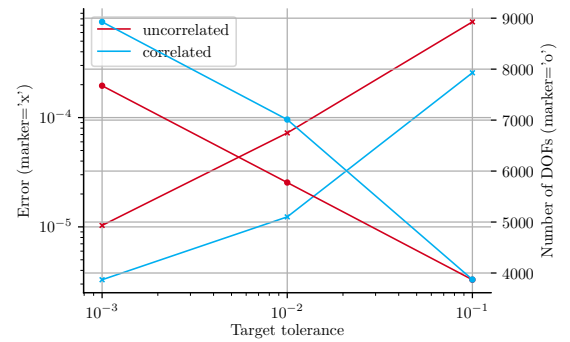


Figure 18 L-Panel example: global relative error in the H^1 -norm against number of degrees of freedom in the ROM. The values are averaged over the number of 20 realizations. The shaded areas indicate the standard deviation of the global relative error.



(a) Number of DOFs and training samples against mean global relative error. The number of training samples is averaged over the number of oversampling problems.



(b) Mean global relative error and number of DOFs against target tolerance $ttol$.

Figure 19 Results for the L-panel example using the maximum number of modes per edge.



Figure 20 Absolute displacement error for different sampling approaches in the deformed placement using 12 fine scale basis functions per edge. In both cases, a scale factor of 10 is used for the deformation and the domain is scaled by the ROM displacement solution.

4.4 | Basis construction and computational time

All simulations, comprising FOM and ROM (offline as well as online), are carried out using a single core (Intel Core i7-10700) and serial implementations. It is noted that the current implementation is not optimized and the provided numbers regarding computation time serve as a proof of concept rather than a rigorous comparison of the computational performance of both models.

Regarding the offline phase, in each of the oversampling problems of all examples, a failure tolerance $\varepsilon_{\text{algofail}} = 1 \cdot 10^{-15}$, and $n_t = 20$ test vectors were used. Furthermore, for the norm induced by the source and range space of the transfer operator, the L^2 and H^1 inner products were used, respectively.

A comparison of the total number of DoFs in the numerical models is given in table 2. In case of the ROM, the number of DoFs and maximum number of fine scale basis functions is averaged over the number of realizations. For each of the investigated examples, the computational time needed to solve the FOM and ROM are given in table 3. With respect to the ROM, the mean over the number of realizations of the assembly time and the time needed to solve the discrete system of equations is given for a fixed number of basis functions. Regarding the time needed to construct the empirical basis, the minimum, maximum and average time over all oversampling problems are averaged over the number of realizations as well.

It is noted that the construction of the local reduced spaces is easily parallelizable since there is no dependency or need to communicate between the different oversampling problems. Hence, the total computational time to evaluate the ROM is estimated by the time needed to construct the local basis for the computationally most expensive oversampling problem (offline phase) and the time to assemble and solve the discrete system of equations for the global problem (online phase). The time needed to precompute the global reduced solution to inform the boundary conditions in the oversampling problem when using the correlated sampling approach, is negligible compared to the runtime of the randomized range finder (rrf) algorithm. Furthermore, in case of the correlated sampling approach, the maximum runtime of algorithm 1 is much higher, compared to the uncorrelated sampling approach. This is due to the repeated computation of the eigenvalues of the covariance matrix Σ as described in section 3.1.4.

The computational time for the online phase of the ROM (using the maximum number of modes per edge) and the FOM comprise the time needed to assemble and solve the system of equations. In case of the block example, the ROM is not favorable, due to the small size of the problem. The ROM (using the correlated sampling approach) is evaluated (using $n = 6$ fine scale modes) at least ≈ 1.5 times faster than the FOM in case of the L-panel example and ≈ 2 times faster in case of the beam example. Depending on the accuracy required for a certain application, the savings in computational time are higher. We also note that — given the computational time needed to solve the FOM — the investigated examples are rather toy problems and that the comparison will be more in favor of the ROM for larger problems.

Table 2 Total number of DoFs of FOM and ROM for the example problems. For the ROM the total number of DoFs is given for a certain number of fine scale edge basis functions per edge (given in paranthesis) to be able to compare the two sampling approaches. Moreover, the average of the (global) maximum number of fine scale edge basis functions is given. The values are averaged over the number of 20 realizations for the block and L-panel example for a target tolerance of $\text{tto1} = 0.001$ and for the beam example for a target tolerance of $\text{tto1} = 0.1$ and $E_a/E_m = 2$.

Example problem	FOM	ROM	
		uncorrelated	correlated
Block	76402.0	492.0 (10 / 29.4)	492.0 (10 / 32.8)
Beam	4204602.0	3925.8 (6 / 12.1)	3923.8 (6 / 15.2)
L-Panel	5042402.0	4522.0 (6 / 22.2)	4522.0 (6 / 34.5)

Table 3 Computational time in seconds for the FOM and ROM. For each sampling approach the minimum (min), maximum (max) and average (avg) runtime of the offline phase for a subdomain — consisting of the runtime of the randomized range finder algorithm (rrf) and the time needed to extend (ext) the edge basis functions into the respective subdomain — are averaged over the number of 10 realizations. The results are reported for the block and L-panel example for a target tolerance of $\text{tto1} = 0.001$ and for the beam example for a target tolerance of $\text{tto1} = 0.1$ and $E_a/E_m = 2$. In case of the online phase, the runtime for the assembly and solution of the discrete system of equations are as well averaged over the number of realizations. Regarding the ROM solution, the number of fine scale edge basis functions is chosen as 10 for the block example, and 6 in case of the beam and L-panel examples.

Example Model	Runtime				
	offline (rrf ext)			online	
	min	max	avg	Assembly	Solve
Block ROM uncorrelated	0.48 0.04	1.32 0.18	0.81 0.08	0.0	0.0
Block ROM correlated	0.61 0.05	2.82 0.38	1.24 0.1	0.0	0.0
Block FOM	-	-	-	0.05	0.53
Beam ROM uncorrelated	1.64 0.18	5.66 0.6	3.49 0.24	0.29	0.1
Beam ROM correlated	1.77 0.19	19.76 0.5	7.84 0.27	0.3	0.11
Beam FOM	-	-	-	2.92	35.79
L-Panel ROM uncorrelated	1.79 0.23	6.54 0.84	4.58 0.39	0.26	0.19
L-Panel ROM correlated	2.17 0.26	38.61 0.99	20.04 0.55	0.26	0.2
L-panel FOM	-	-	-	3.96	53.98

5 | CONCLUSIONS

In this contribution, a methodology to model linear elastic heterogeneous structures is presented. A method combining the variational multiscale method, domain decomposition and model order reduction techniques is developed and applied to model the influence of the fine scale on the coarse scale directly, addressing multiscale problems without a clear separation of scales. Herein, snapshots of the displacement field for local target subdomains are computed by solving an oversampling problem with physically informed — by solving a global reduced problem — correlated as well as uncorrelated random boundary conditions. Based on the displacement snapshots, a fine scale edge basis is constructed and a conforming approximation is obtained by

extending the edge functions into the interior of the respective subdomain. This then allows for a conforming coupling of the reduced coarse grid elements in the framework of standard finite element assembly and hence an easy implementation. The resulting global system of equations is sparse and reduced in size compared to the full order model.

According to the investigated examples, one can obtain a smaller reduction error for the same number of fine scale basis functions when using correlated samples instead of uncorrelated samples. The physically informed boundary conditions in the oversampling problem are shown to improve the approximation capabilities of the reduced local spaces for a small number of basis functions, that is larger target tolerances. Depending on the problem, for both sampling approaches, the pessimistic estimate of the error in the randomized range finder algorithm may lead to the generation of many basis functions for certain subdomains that do not contribute to improving the global error, but result in more accurate approximations for that part of the domain.

This effect seems to be stronger in case of the correlated sampling approach and dependent on the size of the oversampling problem, one has to consider the additional cost due to the repeated computation of the eigenvalues of the covariance matrix in the correlated sampling strategy. Nevertheless, both these issues can be overcome by adapting the error estimate to the multivariate normal distribution and employing an adaptive strategy in which the target tolerance for each local oversampling problem is chosen based on a tolerance on the global error, which was already done in *Example 4* of³⁸ for the GFEM.

Means to include physical states and their variation in the training data is promising in view of the extension of the method to the nonlinear case, which was the motivation for this project and is also subject of future work. In contrast to the linear case, the choice of the correct amplitudes of the boundary data in the oversampling problem or amplitudes of the edge modes when extending these into the respective subdomains poses a great challenge.

Also, the extension to parameterized PDEs and development of an offline/online framework for application in a many-query context (e. g. uncertainty quantification) is interesting. Especially, in applications where e. g. material parameters or the geometry change only in small areas of the domain, the local reduced spaces in the remaining part of the domain might be re-used between different evaluations of the model.

ACKNOWLEDGEMENTS

The authors gratefully acknowledge financial support by the German Research Foundation (DFG), project number 394350870, and by the European Research Council (ERC) under the European Union's Horizon 2020 research and innovation programme (ERC Grant agreement No. 818473).

CODE AVAILABILITY

The complete workflow, i. e. all tasks to process and postprocess the numerical experiments described in this article, are implemented using the automation tool *doit*⁴⁸. The source code necessary to *reproduce* the results is published together with the open source preprint⁴⁹ of this article and publicly available. The numerical experiments are implemented with a self-written code based on the open source computing platform FEniCS⁵⁰.

DATA AVAILABILITY

Data will be made available on request.

References

1. Miehe C, Koch A. Computational micro-to-macro transitions of discretized microstructures undergoing small strains. *Archive of Applied Mechanics (Ingenieur Archiv)* 2002; 72(4-5): 300-317. doi: 10.1007/s00419-002-0212-2
2. Feyel F, Chaboche JL. FE2 multiscale approach for modelling the elastoviscoplastic behaviour of long fibre SiC/Ti composite materials. *Comput. Method. Appl. M.* 2000; 183(3-4): 309-330. doi: 10.1016/s0045-7825(99)00224-8
3. Geers M, Kouznetsova V, Brekelmans W. Computational homogenization. In: Pippan R, Gumbsch P., eds. *Multiscale Modelling of Plasticity and Fracture by Means of Dislocation Mechanics* Vienna: Springer Vienna. 2010 (pp. 327-394)
4. Geers M, Kouznetsova V, Brekelmans W. Multi-scale computational homogenization: Trends and challenges. *J. Comput. Appl. Math.* 2010; 234(7): 2175-2182. doi: 10.1016/j.cam.2009.08.077
5. Yvonnet J, He QC. The reduced model multiscale method (R3M) for the non-linear homogenization of hyperelastic media at finite strains. *J. Comput. Phys.* 2007; 223(1): 341-368. doi: 10.1016/j.jcp.2006.09.019
6. Goury O, Kerfriden P, Bordas S. Bridging analytical and computational homogenisation for nonlinear multiscale problems: A reduced order modelling approach for a damage problem. tech. rep., Cardiff University, School of Engineering; Cardiff, UK: 2014.
7. Hernández J, Oliver J, Huespe A, Caicedo M, Cante J. High-performance model reduction techniques in computational multiscale homogenization. *Comput. Method. Appl. M.* 2014; 276: 149-189. doi: 10.1016/j.cma.2014.03.011
8. Guo T, Rokoš O, Veroy K. Learning constitutive models from microstructural simulations via a non-intrusive reduced basis method. *Comput. Method. Appl. M.* 2021; 384: 113924. doi: 10.1016/j.cma.2021.113924

9. Hashin Z. Analysis of composite materials-a survey. *Journal of Applied Mechanics* 1983; 50: 481-505.
10. Gitman I. *Representative volumes and multi-scale modelling of quasi-brittle materials*. dissertation. Technische Universiteit Delft, Delft, The Netherlands; 2006.
11. Gitman I, Askes H, Sluys L. Representative volume: Existence and size determination. *Eng. Fract. Mech.* 2007; 74(16): 2518-2534. doi: 10.1016/j.engfracmech.2006.12.021
12. Hughes TJ. Multiscale phenomena: Green's functions, the Dirichlet-to-Neumann formulation, subgrid scale models, bubbles and the origins of stabilized methods. *Comput. Method. Appl. M.* 1995; 127(1-4): 387-401. doi: 10.1016/0045-7825(95)00844-9
13. Hughes TJ, Feijóo GR, Mazzei L, Quincy JB. The variational multiscale method—a paradigm for computational mechanics. *Comput. Method. Appl. M.* 1998; 166(1-2): 3-24. doi: 10.1016/s0045-7825(98)00079-6
14. Hou TY, Wu XH. A Multiscale Finite Element Method for Elliptic Problems in Composite Materials and Porous Media. *J. Comput. Phys.* 1997; 134(1): 169-189. doi: 10.1006/jcph.1997.5682
15. Larson MG, Målqvist A. Adaptive Variational Multiscale Methods Based on A Posteriori Error Estimation: Duality Techniques for Elliptic Problems. In: Springer-Verlag. 2005 (pp. 181-193)
16. Larson MG, Målqvist A. Adaptive variational multiscale methods based on a posteriori error estimation: Energy norm estimates for elliptic problems. *Comput. Method. Appl. M.* 2007; 196(21-24): 2313-2324. doi: 10.1016/j.cma.2006.08.019
17. Larson MG, Målqvist A. An adaptive variational multiscale method for convection-diffusion problems. *Commun. Numer. Meth. Engng.* 2009; 25(1): 65-79. doi: 10.1002/cnm.1106
18. Målqvist A, Peterseim D. Localization of elliptic multiscale problems. *Math. Comp.* 2014; 83(290): 2583-2603. doi: 10.1090/s0025-5718-2014-02868-8
19. Altmann R, Henning P, Peterseim D. Numerical homogenization beyond scale separation. *Acta Numer.* 2021; 30: 1-86. doi: 10.1017/s0962492921000015
20. Hesthaven JS, Rozza G, Stamm B. *Certified Reduced Basis Methods for Parametrized Partial Differential Equations*. SpringerBriefs in MathematicsSpringer International Publishing . 2016
21. Quarteroni A, Manzoni A, Negri F. *Reduced Basis Methods for Partial Differential Equations*. 92 of *UNITEXT - La Matematica per il 3+2*. Cham: Springer International Publishing . 2016

22. Prud'homme C, Rovas D, Veroy K, et al. Reliable Real-Time Solution of Parametrized Partial Differential Equations: Reduced-basis Output Bound Methods. *J. Fluids Eng.* 2001; 124(1): 70-80. doi: 10.1115/1.1448332
23. Veroy K, Prud'homme C, Rovas D, Patera A. A Posteriori Error Bounds for Reduced-Basis Approximation of Parametrized Noncoercive and Nonlinear Elliptic Partial Differential Equations. In: AIAA. American Institute of Aeronautics and Astronautics; 2003: 2003-3847
24. Holmes P, Lumley JL, Berkooz G, Rowley CW. *Turbulence, Coherent Structures, Dynamical Systems and Symmetry*. Cambridge Monographs on Mechanics Cambridge University Press . 2009
25. Kunisch K, Volkwein S. Galerkin Proper Orthogonal Decomposition Methods for a General Equation in Fluid Dynamics. *SIAM J. Numer. Anal.* 2002; 40(2): 492-515. doi: 10.1137/s0036142900382612
26. Barrault M, Maday Y, Nguyen NC, Patera AT. An 'empirical interpolation' method: Application to efficient reduced-basis discretization of partial differential equations. *Cr. Math.* 2004; 339(9): 667-672. doi: 10.1016/j.crma.2004.08.006
27. Chaturantabut S, Sorensen DC. Nonlinear Model Reduction via Discrete Empirical Interpolation. *SIAM J. Sci. Comput.* 2010; 32(5): 2737-2764. doi: 10.1137/090766498
28. Ryckelynck D. A priori hyperreduction method: An adaptive approach. *J. Comput. Phys.* 2005; 202(1): 346-366. doi: 10.1016/j.jcp.2004.07.015
29. Ryckelynck D. Hyper-reduction of mechanical models involving internal variables. *Int. J. Numer. Meth. Engng* 2009; 77(1): 75-89. doi: 10.1002/nme.2406
30. Farhat C, Avery P, Chapman T, Cortial J. Dimensional reduction of nonlinear finite element dynamic models with finite rotations and energy-based mesh sampling and weighting for computational efficiency. *Int. J. Numer. Meth. Engng* 2014; 98(9): 625-662. doi: 10.1002/nme.4668
31. Farhat C, Chapman T, Avery P. Structure-preserving, stability, and accuracy properties of the energy-conserving sampling and weighting method for the hyper reduction of nonlinear finite element dynamic models. *Int. J. Numer. Meth. Engng* 2015; 102(5): 1077-1110. doi: 10.1002/nme.4820
32. Hernández J, Caicedo M, Ferrer A. Dimensional hyper-reduction of nonlinear finite element models via empirical cubature. *Comput. Method. Appl. M.* 2017; 313: 687-722. doi: 10.1016/j.cma.2016.10.022
33. Guo M, Hesthaven JS. Reduced order modeling for nonlinear structural analysis using Gaussian process regression. *Comput. Method. Appl. M.* 2018; 341: 807-826. doi: 10.1016/j.cma.2018.07.017

34. Raissi M, Perdikaris P, Karniadakis G. Physics-informed neural networks: A deep learning framework for solving forward and inverse problems involving nonlinear partial differential equations. *J. Comput. Phys.* 2019; 378: 686-707. doi: 10.1016/j.jcp.2018.10.045
35. Buhr A, Iapichino L, Ohlberger M, Rave S, Schindler F, Smetana K. *6 Localized model reduction for parameterized problems*: 245–306; De Gruyter . 2020
36. Babuška I, Lipton R. Optimal Local Approximation Spaces for Generalized Finite Element Methods with Application to Multiscale Problems. *Multiscale Model. Simul.* 2011; 9(1): 373-406. doi: 10.1137/100791051
37. Smetana K, Patera AT. Optimal Local Approximation Spaces for Component-Based Static Condensation Procedures. *SIAM J. Sci. Comput.* 2016; 38(5): A3318-A3356. doi: 10.1137/15m1009603
38. Buhr A, Smetana K. Randomized Local Model Order Reduction. *SIAM J. Sci. Comput.* 2018; 40(4): A2120-A2151. doi: 10.1137/17m1138480
39. Iapichino L, Quarteroni A, Rozza G. Reduced basis method and domain decomposition for elliptic problems in networks and complex parametrized geometries. *Comput. Math. Appl.* 2016; 71(1): 408-430. doi: 10.1016/j.camwa.2015.12.001
40. Zienkiewicz O, Taylor R. *The Finite Element Method Volume 1: The Basis*. Oxford: Butterworth-Heinemann. 5th ed. 2000.
41. Babuška I, Caloz G, Osborn JE. Special Finite Element Methods for a Class of Second Order Elliptic Problems with Rough Coefficients. *SIAM J. Numer. Anal.* 1994; 31(4): 945-981. doi: 10.1137/0731051
42. Babuška I, Melenk J. The Partition Of Unity Method. *Int. J. Numer. Meth. Engng.* 1997; 40(4): 727-758. doi: 10.1002/(sici)1097-0207(19970228)40:4<727::aid-nme86>3.0.co;2-n
43. Babuška I, Banerjee U, Osborn JE. Generalized Finite Element Methods — Main Ideas, Results And Perspective. *Int. J. Comput. Methods* 2004; 01(01): 67-103. doi: 10.1142/s0219876204000083
44. Bertram A, Glüge R. *Solid Mechanics*. Springer International Publishing . 2015
45. Eftang JL, Patera AT. Port reduction in parametrized component static condensation: approximation and a posteriori error estimation. *International Journal for Numerical Methods in Engineering* 2013; 96. doi: 10.1002/nme.4543
46. Unger JF, Eckardt S. Multiscale Modeling of Concrete. *Arch Computat Methods Eng* 2011; 18(3): 341-393. doi: 10.1007/s11831-011-9063-8
47. Lee NS, Bathe KJ. Effects of element distortions on the performance of isoparametric elements. *Int. J. Numer. Meth. Engng.* 1993; 36(20): 3553-3576. doi: 10.1002/nme.1620362009

48. Schettino EN. pydoit/doi: task management & automation tool (python). <https://doi.org/10.5281/zenodo.4892136>; 2021
49. Diercks P, Veroy K, Robens-Radermacher A, Unger JF. Multiscale modeling of linear elastic heterogeneous structures based on a localized model order reduction approach. <https://arxiv.org/abs/2201.10374>; 2022.
50. Alnæs MS, Blechta J, Hake J, et al. The FEniCS Project Version 1.5. *Archive of Numerical Software* 2015; 3(100). doi: 10.11588/ans.2015.100.20553

How to cite this article: P. Diercks, K. Veroy, A. Robens-Radermacher, and J. F. Unger (2023), Multiscale modeling of linear elastic heterogeneous structures via localized model order reduction, *International Journal for Numerical Methods in Engineering*, 2023;XX:X-X.